A Microbial Induced Synthesis of Hydroxyapatite with High UV Light Photocatalytic Activity for Tetracycline Degradation

Ting Zeng
Southwest University of Science and Technology
Yujie Yan
Southwest University of Science and Technology
Juan Shen (sj-shenjuan@163.com)
Southwest University of Science and Technology
Ke Chen
Southwest University of Science and Technology
Mi Tang
Southwest University of Science and Technology
Rigui Chen
Southwest University of Science and Technology
Zhicheng Guo
Southwest University of Science and Technology
Bisheng Tan
China Academy of Engineering Physics Institute of Chemical Materials
Bo Jin
Southwest University of Science and Technology

Research Article

Keywords: hydroxyapatite, bacterial induction, photocatalysis, tetracycline hydrochloride, Density functional theory

Posted Date: December 10th, 2021

DOI: https://doi.org/10.21203/rs.3.rs-1014827/v1

Abstract

More and more new materials have been developed, but the research on the development and utilization of the single-phase materials has been neglected. Assembled from nano-particles, a high specific surface area and porous hydroxyapatite (BI-HA) has been synthesized by feasible bacterial induction. The surface structure and morphology of the nanocomposites were characterized by Brunauer–Emmett–Teller (BET) apparatus, X-ray diffraction (XRD), transmission electron microscopy (TEM). The results suggest the obtained BI-HA powder with porous morphology, which were composed of nanoparticles with (100) crystal plane. The photoactivity of different HA samples was evaluated by the photocatalytic degradation of tetracycline hydrochloride (TC). The HA with (100) crystal plane displayed an obviously enhanced photocatalytic activity (75.33–86.43% for 60 min). Combined with experiments and DFT calculations, for the BI-HA with (100) crystal plane, it displayed better photocatalytic performance for photodegradation of TC. This study provides a viewpoint to fabricate high-performance nonmetal photocatalyst for wastewater treatment.

1. Introduction

Tetracycline (TC) is often detected from groundwater, surface water and sewage treatment systems as a new source of water pollution. It has caused "pseudo-persistence" pollution to water bodies, leading to an increase in drug-resistant pathogenic microorganisms, which has aroused widespread concern (Zhou et al. 2020; Islam et al. 2019; Du et al. 2019). In recent years, physical and chemical methods, biological treatment methods, and chemical treatment methods have been devoted into the removal of TC from wastewater (Qu et al. 2020; Zhao et al. 2019). Among them, photocatalysis technology, as an advanced oxidation technology, has the advantages of utilizing the potential advantages of sunlight and high processing efficiency, and is used for the treatment of refractory organic pollutants (Khodadadi et al. 2019; Zhang et al. 2020; Wang et al. 2017). However, there are not many reports on the degradation of antibiotics by photocatalytic technology, so it is necessary to intensify efforts to explore the use of photocatalytic technology to treat antibiotic wastewater(Yu et al. 2019; Wei et al. 2020).

Hydroxyapatite (HA), which is the main inorganic component in bone and enamel, has the advantages of good biocompatibility, safety and non-toxicity, and is therefore widely used in biomedical materials (Yadav et al. 2020; Farraris et al. 2020; He et al. 2019), drug carriers (Yi et al. 2016; Xiong et al. 2016) and catalysts (Schiavoni et al. 2018; Shariffuddin et al. 2013). At the same time, due to the simple preparation process and low cost of HA, it is also widely used in the fields of catalyst carrier and water body repair. However, the photocatalytic activity of HA is still much lower than expected because of its poor charge transport, slow redox reaction kinetics, and low carrier mobility. Therefore, the development of a modification strategy to improve the HA charge kinetics is essential for achieving high performance HA (Reeta Mary et al. 2018; Valizadeh et al. 2014; Ekka et al. 2018; Lv et al. 2019; Jiraborvornpongsa et al. 2019; Huang et al. 2017). At present, several modification strategies have been shown to improve the photocatalytic efficiency of HA, including material design and preparation(Reeta Mary et al. 2018), cocatalyst deposition (Lv et al. 2019) and elemental doping (jiraborvornpongsa et al. 2019; Ishisone et al.

2020). Several groups have reported that synthetic HA has better degradation properties of organic dyes by controlling the preparation conditions of hydroxyapatite. Nathanael et al. prepared a TiO_2-HAP composite by high-speed centrifugal gravity mixing of hydroxyapatite and $Ti(OH)_4$ colloids (Joseph Nathanael et al. 2010). Compared with hydroxyapatite or TiO_2 alone, the composite catalyst was under ultraviolet light. It has better degradation ability to methyl orange. Reddy et al. used hydroxyapatite to degrade calcium and magnesium indicators under ultraviolet light, which can remove 92% of COD and improve the biodegradability of dye wastewater (Reddy et al. 2007). They believe that UV irradiation can change the electronic structure of PO_4^{3-} on the surface of hydroxyapatite, generate oxygen vacancies and active $\bullet O_2^-$, and then degrade dye molecules. Although the research on the degradation of pollutants using hydroxyapatite composite photocatalyst has made some progress, there are some disadvantages. For example, hydroxyapatite can only be used as a support, and only plays an auxiliary role in the photocatalytic process. The preparation process of HA composite catalyst is complicated and their structure is unstable. Generally, the prepared composite catalyst can only be used under ultraviolet irradiation. Although the introduction of precious metals can increase the visible light activity of composite materials, it also increases manufacturing costs. Based on the characteristics of hydroxyapatite with different surface activity, the development of highly active hydroxyapatite photocatalyst has certain theoretical significance and practical value.

Here, HA particles were first prepared by using a novel bacterial induction method. The crystal structure, morphological characteristics, and specific surface area of HA particles were studied, and the photocatalysis of the prepared HA particles on the degradation of tetracycline (TC) under ultraviolet light was studied. This synthesis method is different from the conventional synthesis methods. Phosphatase can be released by Bacillus subtilis to control apatite mineralization. A large number of fine-pored, high specific surface area HA crystal materials are surprisingly obtained. HA itself has good photocatalytic activity, and it does not need to add other photosensitive materials to enhance its photocatalytic performance. In addition, the intrinsic relationship between crystal morphological characteristics and photocatalytic activity of HA was preliminarily discussed. This work provided a simple method for improving the photocatalytic activity of HA, and also deepened the understanding of the photocatalytic mechanism of phosphate photocatalysts.

2. Materials And Methods

2.1 Materials

Disodium phenyl phosphate dihydrate ($C_6H_5PO_4Na_2{\cdot}2H_2O$) was obtained from Aladdin (Shanghai, China), $CaCl_2$, HCl, NaCl, and NaOH were purchased from Kelong Chemical Inc (Sichuan, China), and all were analytical grade. Yeast powder and peptone were purchased from Beijing Aoboxing Bio-Tech Co., Ltd (Beijing, China), and both were biological reagent. *Bacillus subtilis* was purchased from China General Microbiological Culture Collection Center. Deionized water was used in all experiments.

2.2 Synthesis of hydroxyapatite

HA was synthesized by following steps. The first step, Luria-Bertani (LB) liquid medium was prepared and conducted by high pressure steam sterilization. The second step, the activated *Bacillus subtilis* was inoculated into LB medium (V/V = 10%), and cultured in air bath oscillator under 37 ^{o}C for a certain time to obtain bacteria solution with different concentration. The last step, $CaCl_2$ and $C_6H_5PO_4Na_2$ (Ca/P = 1.67) were dissolved completely in deionized water at room temperature, and the solution was conducted by sterilization. And the obtained solution was added into the above bacteria solution under a clean bench, and the mixture was cultured in air bath oscillator under 37 ^{o}C for 12 h. The obtained products were washed with ethyl alcohol and deionized water, and freeze dried for 24 h.

2.3 Characterization

The crystal structures of products were determined through X-ray powder diffraction (XRD; DMAX1400; Rigaku; Japan) with Cu Kα radiation, $2\theta = 3–80°$. The images of the particle morphology and of the products were obtained using a scanning electron microscope (SEM; TM-4000; Hitachi; Japan) and transmission electron micro-144 scopy (TEM; Zeiss Libra 200FE; Germany). Fourier transform infrared spectroscopy (FT-IR; Nicolet-6700; PerkinElmer; America) in transmittance mode was used within the range of 400–4000 cm^{-1} to identify the functional groups. Nitrogen adsorption–desorption isotherms were measured with an automatic surface area and porosity analyzer (AUTOSORB-1-C, Quantachrome, America) at the temperature of liquid nitrogen. The pore size distributions were derived from the adsorption branches of the isotherms using BJH theory. The particle size distribution of the as-synthesized powder was analyzed by using a laser particle size analyzer (90 plus; Brookhaven Instruments Corporation; America). The values of pH at the point of zero charge (pH pzc) of HA were analyzed using Zeta Potential Analyzer Zeta potential (zetaPALS; Brookhaven; America).

2.4 Photocatalytic experiments

The TC degradation activity of the as-prepared HA samples was measured under 300 W mercury lamp. Typically, 13.0 mg catalyst was dispersed in 50 mL aqueous solution containing TC with an initial concentration of 10 mg L^{-1}. The mixed solution was placed in the reactor, and the magnetic stirring was carried out for 30 min under the dark environment to reach an equilibrium of adsorption and desorption. At given time intervals, 5 mL solution was taken out every 15 min and centrifuged (4000 rpm, 5 min) to remove the catalyst. The concentration of supernatant was then measured using the UV–vis spectrometer.

2.5 Computational details

All DFT calculations were performed by using the Vienna ab initio simulation package (VASP). The generalized gradient approximation (GGA) with Perdew-Burker-Ernzerhof (PBE) functional was applied to address the nonlocal exchange correlation energy. DFT method with the U_{eff} = 5.0 eV was used in all calculations (Yang et al. 2009). The kinetic cutoff energy of 600 eV was adopted, and the Brillouin zone integration was sampled with the 2 × 2 × 3 k-point mesh. Structure optimization was deemed as

converged until the force of all atoms less than 0.03 eV/Å, and the criteria of energy convergence was set to 1×10^{-5} eV.

3. Results And Discussion

3.1 Material characterization

The mechanism of BI-HA synthesis is presented in Figure 1. The morphologies of the as-prepared samples were investigated by SEM and (HR)TEM techniques. Figure 1 shows the SEM images of the products. Figures 2a and 2b indicate that the morphology of the products was of nanoparticles when the Ca^{2+} concentrations were 0.01 and 0.03 mol L^{-1}. When the Ca^{2+} concentration was 0.05 mol L^{-1}, these sheets were combined into uniform porous shapes with a rough surface (Figure 2c). Meanwhile, the Ca^{2+} concentration was 0.10 mol L^{-1} (Figure 2d), the obtained BI-HA with porous morphology, which were composed of nanoparticles. The TEM and HRTEM images of nanoparticles in Fig. 2d is displayed in Figs. 2e and 2f. The morphology was sheet-like and consisted of nanoparticles. The lattice spacing of 0.27nm agreed with the distance between two (300) planes of BI-HA.

The crystal structure of as-prepared catalysts was thoroughly investigated by X-ray diffraction (XRD). The XRD patterns of the products prepared under different Ca^{2+} concentrations are shown in Figure 3. The characteristic peaks in Figures 3(a–d) remained consistent with the BI-HA according to the JCPDS card (NO. 09-0432), thereby indicating that the product was successfully converted into BI-HA. Figures 3b and 3c present the characteristic peaks of the standard card and the increase in intensity, thereby indicating that the high concentration of bacterial solution was conducive to BI-HA production. The phenomenon can be interpreted for the production of phosphatase during the metabolism of *B. subtilis* (Molla et al. 1984). Disodium phenyl phosphate, as a substrate, slowly released PO_4^{3-} to the solution under the action of phosphatase. Then, the PO_4^{3-} and Ca^{2+} from the solution reacted to form porous BI-HA crystals under suitable conditions.

The FT-IR spectra of disodium phenyl phosphate dihydrate and the products prepared under different bacterial concentrations are presented in Figure 4. Figure 4a shows the FT-IR spectrum of $C_6H_5PO_4Na_2{\cdot}2H_2O$. The CH stretching modes for monosubstituted benzene were found in the region 3105–2900 cm^{-1}. The bands at 1596, 1489 and 1238 cm^{-1} were assigned as benzene ring-stretching modes. The bands observed at 1159 and 1115 cm^{-1} were assigned to the asymmetric stretching vibrations. Bands at 1009 and 995 cm^{-1} were assigned to the PO_4 symmetric stretching vibrations. The bands at 886, 763 and 734 cm^{-1} were assigned as the out-of-plane CH deformations of the phenyl ring (Anto et al. 2010). Compared with Figure 4a, the adsorption bands of Figures 4b-4e were not consistent with Figure 4a. The BI-HA characteristic peaks appeared in the FT-IR spectra shown in Figures 4 (b and e). The wide absorption bands at ca. 3434 and 1633 cm^{-1} are attributed to the adsorbed water. The absorption peak at 1427 cm^{-1} may be caused by the carbon dioxide in the aqueous solution or air. The

peaks at 1113 (v_3), 1092 (v_3), 963(v_1), 602 (v_4), and 564 cm^{-1} (v_4) are the characteristic bands for PO_4^{3-}. This phenomenon demonstrated that the addition of *Bacillus subtilis* solution could favor the formation of BI-HA products.

As presented in Figure 5, the nitrogen adsorption and desorption isotherms and the pore size distribution curves of the product were investigated. According to the IUPAC classification, all the isotherms in Figures 5a-5d were assigned to types IV and H3 hysteresis loops, thereby confirming the existence of mesopores. Figures 5a1-5d1 showed that the pore size distribution was irregular and comprised a mixture of mesopores and micropores. As the concentration of Ca^{2+} changed from 0.01 mol L^{-1} to 0.1 mol L^{-1}, the specific surface area of the product changed from 133.8 m^2 g^{-1}, 173.8 m^2 g^{-1}, 196.7 m^2 g^{-1}, to 73.61 m^2 g^{-1}. Meanwhile, the pore structure of the product mainly composed of mesopores according to the analysis of the total pore and mesoporous volumes.

3.2 Photocatalytic degradation of TC

In order to evaluate the photocatalytic activity of different synthetic BI-HA powders, the degradation of TC using BI-HA1, BI-HA2, BI-HA3 and BI-HA4 were tested under UV light irradiation. Firstly, due to the larger specific surface area of the prepared hydroxyapatite samples, the C/C_0 ratio under dark reaction conditions for 75 minutes was studied. As shown in Fig. 6a, lower than 22% TC was adsorbed onto the as-prepared photocatalysts in the dark, indicating relatively poor adsorption capacity of TC over these samples. Under UV light irradiation, the blank experiment test revealed that the self-degraded of TC is nearly negligible shown in Fig. 6b. The BI-HA photocatalysts displayed a good photocatalytic activity (74.4~86.4% for 60 min) for TC degradation. Among those samples, BI-HA4 showed the highest photocatalytic efference (86.4%) after 60 min.

3.3 Possible photocatalytic mechanism

The development of photocatalytic materials has thus been an important requirement. Various types of materials ranging from natural inorganic materials to organic polymers have received a remarkable interest for degradating TC from solution (Lyu et al. 2019; Zhang et al. 2019; Xiong et al. 2017). This research is different from previous synthetic ideas. A novel synthetic method to simulate the microbial biomineralization in nature is used, and hydroxyapatite crystals with a large specific surface area were obtained (Table 1). It consists of nanoscale ultrafine particles and their dense aggregates (Fig. 2). The BI-HA samples exhibited enhanced photocatalytic performance by photocatalytic degradation of TC under UV light irradiation. Structures always show great influence on the absorption of solar energy and transfer of photogenerated electron-hole paries (Zhang et al. 2018; Peng et al. 2016). HRTEM result showed the synthetic BI-HA nanoparticle with the platelet crystal growth direction was (100). For the comparison of the photocatalytic degradation effects of TC with (100) or (001) crystal plane HA samples, we selected different HA samples for TC photodegradation experiments (Table 1). As shown in Fig. 7, HA photocatalysts with different crystallite structures and morphologies displayed different photocatalytic activity. The HA with (100) crystal plane displayed an obviously enhanced photocatalytic activity (75.33–86.43% for 60 min), while the HA with (001) crystal plane exhibited poor photocatalytic degradation

effiency (18.0 % for 60 min) for TC degradation. It shows that as-prepared BI-HA4 has a high degradation capacity, thereby indicating that BI-HA4 with a (100) crystal plane, a specific morphology and specific surface is of great significance in photocatalytic activity.

Table 1 Comparison of different morphologies and specific surface area hydroxyapatite photocatalytic values

HA synthetic method	Specific surface area (m^2 g^{-1})	Crystal growth crystal face	Photocatalytic value (%)	Morphology	Synthetic method Ref.
Bacterial -induced method (BI-HA)	73.61	(100)	86.43	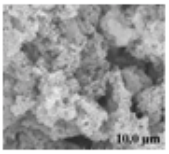	Current work
Double interfacial diffusion method (DID-HA)	188.5	(100)	75.33	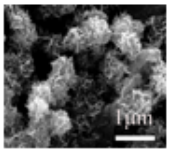	Xia et al. 2019
Hydrothermal method (Hy-HA1)	130.8	(100)	80.14	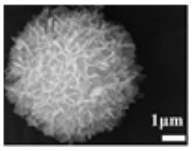	Qi et al. 2016
Hydrothermal method (Hy-HA2)	–	(001)	54.77	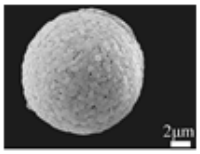	Qi et al. 2015
Hard template method (HT-HA1)	Ball-shaped 201.3	(001)	55.72	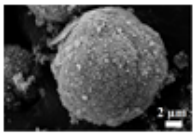	Xia et al. 2018
Hard template method (HT-HA2)	Rod-shaped 190.9	(001)	47.20	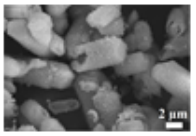	Xia et al. 2018
Hard template method (HT-HA3)	Block-shaped 106.3	(001)	51.70	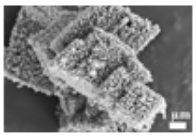	Xia et al. 2018
Double surfactants method (DS-HA)	–	(001)	20.76	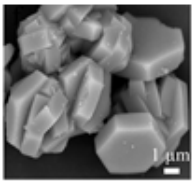	Chen et al. 2020

Under the action of HA, UV light excites the H_2O or O_2 molecules in the surrounding air to produce $\bullet OH^-$ and $\bullet O_2^-$. After UV excitation, the electrons are transferred to O_2 to form $\bullet O_2^-$, while $\bullet OH^-$ may be due to

the reaction of $\cdot O_2^-$ and H_2O. These free radicals can effectively decompose Tetracycline, etc., to generate CO_2, H_2O and other hydrocarbon compounds.

Under the catalysis of HA, tetracycline will react as follows:

$$HA + h\nu \rightarrow HA^{\bullet} \quad (1)$$
$$HA^{\bullet} + O_2 \rightarrow HA + \cdot O_2^- \quad (2)$$
$$\cdot O_2^- + H_2O \rightarrow \cdot OH^- \quad (3)$$
$$\cdot OH^- + \cdot O_2^- + TC \rightarrow \text{degradation products } (CO_2, C_nH_n, \text{etc.}) \quad (4)$$

We know that the photoinduced electron/hole depends largely on the energy band structure and electronic density of state (DOS) of photocatalyst (Zhang et al. 2018). As shown in Figures 8a and 8b, the valence band (VB) of HA is mainly contributed by the O-2p orbit below Fermi level, while the conduction band (CB) is attributed to the Ca-4s orbit above Fermi level. However, due to the derivative discontinuity of the exchange correlation function, the bandgap (E_g) is underestimated by using DFT calculation (Song et al. 2016). The existence of HA (100) effectively reduces the band gap. Compared with HA (001) in Figure 8a, the VB width of HA (100) is increased. Therefore, the separation of photoinduced electrons in HA (100) will be enhanced, which indicates a better photocatalytic oxidation ability (Pan et al. 2014).

4. Conclusion

The HA photocatalysts had been obtained through a *Bacillus subtilis* induction method with special flower-like structure were obtained. The obtained BI-HA with porous morphology self-assembled by sheets, which were composed of nanoparticles, had an average particle size of 0.66 μm and a high specific surface area. For the BI-HA with (100) crystal plane, it displayed better photocatalytic performance for photodegradation of TC. High reactive sites on the HA made it an effective photocatalyst for degradation of TC (above 86%). The BI-HA powder with (100) crystal plane shows dramatic photocatalytic activity, confirming their practical use in water purification.

Declarations

Acknowledgements

This work was financially supported by National Natural Science Foundation of China (No. 21201142), the basic research project of Sichuan Province for Science and Technology Development (No. 2019YJ0355), Outstanding Youth Science and Technology Talents Program of Sichuan (No. 19JCQN0085), Key Projects of the Pre-research Fund of the General Armament Department (No. 6140720020101) and National Defense Technology Foundation Project (No. JSJL2016404B002).

The authors declare that they have no known competing financial interests or personal relationships that could have appeared to influence the work reported in this paper.

The authors declare the following financial interests/personal relationships which may be considered as potential competing interests:

Ethics approval and consent to participate: Not applicable

Consent for publication: Not applicable

Funding: National Natural Science Foundation of China(No. 21201142)

Availability of data and materials

Data availability statements can take one of the following forms (or a combination of more than one if required for multiple datasets):

- The datasets generated and/or analysed during the current study are available in the [NAME] repository, [PERSISTENT WEB LINK TO DATASETS]
- The datasets used and/or analysed during the current study are available from the corresponding author on reasonable request.
- All data generated or analysed during this study are included in this published article [and its supplementary information files].
- The datasets generated and/or analysed during the current study are not publicly available due [REASON WHY DATA ARE NOT PUBLIC] but are available from the corresponding author on reasonable request.
- Data sharing is not applicable to this article as no datasets were generated or analysed during the current study.
- The data that support the findings of this study are available from [third party name] but restrictions apply to the availability of these data, which were used under license for the current study, and so are not publicly available. Data are however available from the authors upon reasonable request and with permission of [third party name].
- Not applicable. If your manuscript does not contain any data, please state 'Not applicable' in this section.

Author contributions: Please check the Instructions for Authors of the Journal that you are submitting to for specific instructions regarding contribution statements.
In absence of specific instructions and in research fields where it is possible to describe discrete efforts, the Publisher recommends authors to include contribution statements in the work that specifies the contribution of every author in order to promote transparency. These contributions should be listed at the end of the submission.

Examples of such statement(s) are shown below:Free text:

All authors contributed to the study conception and design. Material preparation, data collection and analysis were performed by [full name], [full name] and [full name]. The first draft of the manuscript was written by [full name] and all authors commented on previous versions of the manuscript. All authors read and approved the final manuscript.

Example CRediT taxonomy:

Role	Definition
Ting Zing	Ideas; formulation or evolution of overarching research goals and aims.
Zhicheng Guo	Management activities to annotate (produce metadata), scrub data and maintain research data (including software code, where it is necessary for interpreting the data itself) for initial use and later re-use.
Bisheng Tan	Application of statistical, mathematical, computational, or other formal techniques to analyse or synthesize study data.
Juan Shen	Acquisition of the financial support for the project leading to this publication.
Ting Zing, Mi Tang, Yujie Yan	Conducting a research and investigation process, specifically performing the experiments, or data/evidence collection.
Bisheng Tan	Development or design of methodology; creation of models.
Ting Zing	Management and coordination responsibility for the research activity planning and execution.
Juan Shen	Provision of study materials, reagents, materials, patients, laboratory samples, animals, instrumentation, computing resources, or other analysis tools.
Zhicheng Guo, Bisheng Tan	Programming, software development; designing computer programs; implementation of the computer code and supporting algorithms; testing of existing code components.
Juan Shen, Bo Jin	Oversight and leadership responsibility for the research activity planning and execution, including mentorship external to the core team.
Ting Zeng, Yujie Yan, Ke Chen	Verification, whether as a part of the activity or separate, of the overall replication/reproducibility of results/experiments and other research outputs.
Bisheng Tan	Preparation, creation and/or presentation of the published work, specifically visualization/data presentation.
Ting Zeng	Preparation, creation and/or presentation of the published work, specifically writing the initial draft (including substantive translation).
Ting Zeng, Juan Shen	Preparation, creation and/or presentation of the published work by those from the original research group, specifically critical review, commentary or revision – including pre- or post-publication stages.

References

1. Anto PL, Anto RJ, Varghese HT, Panicker CY, Philip D (2010). **Vibrational spectroscopic studies and ab initio calculations of phenyl phosphate disodium salt.** J. Raman Spectrosc., 41 , pp. 113-119.
2. Chen R, Shen J (2020). **The synthesis of hydroxyapatite crystals with various morphologies via the solvothermal method using double surfactants.** Mater. Lett., 259 , pp. 126881.
3. Du B, Yang Q, Li X, Yuan W, Chen Y, Wang R (2019). **Impacts of long-term exposure to tetracycline and sulfamethoxazole on the sludge granules in an anoxic-aerobic wastewater treatment system.** Sci. Total. Environ., 684, pp. 67-77.
4. Ekka B, Nayak SR, Achary LSK, Sarita, Kumar A, Mawatwal S, Dhiman R, Dash P, Patel RK (2018). **Synthesis of hydroxyapatite-zirconia nanocomposite through sonochemical route: A potential catalyst for degradation of phenolic compounds.** J. Environ. Chem. Eng., 6 , pp. 6504-6515.
5. Ferraris S, Yamaguchi S, Barbani N, Cazzola M, Cristallini C, Miola M, Vernè E, Spriano S (2020). **Bioactivematerials: In vitro investigation of different mechanisms of hydroxyapatite precipitation.** Acta Biomaterialia, 102 , pp. 468-480.
6. He F, Springer NL, Whitman MA, Pathi SP, Lee Y, Mohanan S, Marcott S, Chiou AE, Blank BS, Iyengar N, Morris PG, Jochelson M, Hudis CA, Shah P, Kunitake JAMR, Estroff LA, Lammerding J, Fischbach C (2019). **Hydroxyapatite mineral enhances malignant potential in a tissue-engineered model of ductal carcinoma in situ (DCIS).** Biomaterials, 224 , pp. 119489.
7. Huang J, Gong Y, LiuY, Suo X, Li H (2017). **Developing titania-hydroxyapatite-reduced graphene oxide nanocomposite coatings by liquid flame spray deposition for photocatalytic applications.** J. Eur. Ceram. Soc., 37), pp. 3705-3711.
8. Ishisone K, Jiraborvornpongsa N, Isobe T, Matsushita S, Wakumura M, Oshikiri M, Nakajima A (2020). **Experimental and theoretical investigation of WO_x modification effects on the photocatalytic activity of titanium-substituted hydroxyapatite.** Appl. Catal. B: Environ., 264 , pp. 118516.
9. Islam GM, Gilbride KA (2019). **The effect of tetracycline on the structure of the bacterial community in a wastewater treatment system and its effects on nitrogen removal.** J. Hazard. Mater., 371, pp. 130-137.
10. Jiraborvornpongsa N, Isobe T, Matsushita S, Yamaguchi A, Miyauchi M, Wakamura M, Nakajima A (2019). **Effects of MoO_x modification on photocatalytic activity of hydroxyapatite and Ti-doped hydroxyapatite.** Adv. Powder Technol., 30 , pp. 1617-1624.
11. Joseph Nathanael A, Mangalaraj D, Chen PC, Ponpandian N (2010). **Mechanical and photocatalytic properties of hydroxyapatite/titania nanocomposites prepared by combined high gravity and hydrothermal process.** Compos. Sci. Technol., 70 , pp. 419-426.
12. Khodadadi M, Hossein Panahi A, Al-Musawi TJ, Ehrampoush MH, Mahvi AH (2019). **The catalytic activity of $FeNi_3@SiO_2$ magnetic nanoparticles for the degradation of tetracycline in the heterogeneous Fenton-like treatment method.** Journal of Water Process Engineering, 32, pp. 100943.
13. Lu J, Song J, Niu H, Pan L, Zhang X, Wang L, Zou JJ (2016). **Periodic density functional theory study of ethylene hydrogenation over Co_3O_4 (111) surface: The critical role of oxygen vacancies.** Appl. Surf. Sci., 371, pp. 61-66.

14. Lyu J, Hu Z, Li Z, Ge M (2019). **Removal of tetracycline by BiOBr microspheres with oxygen vacancies: Combination of adsorption and photocatalysis.** J. Phys. Chem. Solids, 129 , pp. 61-70.
15. Lv C, Liang H, Chen H, Wu L (2019). **Hydroxyapatite supported Co_3O_4 catalyst for enhanced degradation of organic contaminants in aqueous solution: Synergistic visible-light photo-catalysis and sulfate radical oxidation process.** Microchem. J., 149 , pp. 103959.
16. Molla MAZ, Chowdhury AA, Islam A, Hoque S (1984). **Microbial mineralization of organic phosphate in soil.** Plant Soil, 78 , pp. 393-399.
17. Pan L, Wang S, Mi W, Song J, Zou JJ, Wang L, Zhang X (2014). **Undoped ZnO abundant with metal vacancies.** Nano Energy, 9 , pp. 71-79.
18. Peng C, Yang X, Li Y, Yu H, Wang H, Peng F (2016). **Hybrids of Two-Dimensional Ti_3C_2 and TiO_2 Exposing {001} Facets toward Enhanced Photocatalytic Activity.** Acs Appl. Mater. Interfaces, 8, pp. 6051-6060.
19. Qi YC, Shen J, Jiang QY, Jin B, Chen JW, Zhang X, Su JL (2016). **Hierarchical porous hydroxyapatite microspheres: synthesis and application in water treatment.** J. Mater. Sci., 51 , pp. 2598-2607.
20. Qi Y, Shen J, Jiang Q, Jin B, Chen J, Zhang X (2015). **The morphology control of hydroxyapatite microsphere at high pH values by hydrothermal method.** Adv. Powder Technol., 26 , pp. 1041-1046.
21. Qu Z, Dong G, Zhu S, Yu Y, Huo M, Xu K, Liu M (2020). **Recycling of groundwater treatment sludge to prepare nano-rod erdite particles for tetracycline adsorption.** J. Clean. Prod., 257 , pp. 120462.
22. Reeta Mary I, Sonia S, Navadeepthy D, Mangalaraj D, Viswanathan C, Ponpandian N (2018). **Surfactant-free solvothermal synthesis of Hydroxyapatite nested bundles for the effective photodegradation of cationic dyes**J. Phys. Chem. Solids, 116 , pp. 180-186.
23. Reddy MP, Venugopal A, Subrahmanyam M (2007). **Hydroxyapatite photocatalytic degradation of calmagite (an azo dye) in aqueous suspension.** Appl. Catal. B: Environ., 69, pp. 164-170.
24. Schiavoni M, Campisi S, Carniti P, Gervasini A, Delplanche T (2018). **Focus on the catalytic performances of Cu-functionalized hydroxyapatites in NH_3-SCR reaction.** Appl. Catal. A: Gen., 563, pp. 43-53.
25. Shariffuddin JH, Jones MI, Patterson DA (2013). **Greener photocatalysts: Hydroxyapatite derived from waste mussel shells for the photocatalytic degradation of a model azo dye wastewater.** Chem. Eng. Res. Des., 91 , pp. 1693-1704.
26. Valizadeh S, Rasoulifard MH, Dorraji MSS (2014). **Modified $Fe_3O_4^-$ hydroxyapatite nanocomposites as heterogeneous catalysts in three UV, Vis and Fenton like degradation systems.** Appl. Surf. Sci., 319 , pp. 358-366.
27. Wang X, Jia J, Wang Y (2017). **Combination of photocatalysis with hydrodynamic cavitation for degradation of tetracycline.** Chem. Eng. J., 315, pp. 274-282.
28. Wei X, Feng H, Li L, Gong J, Jiang K, Xue S, Chu PK (2020). **Synthesis of tetragonal prismatic γ-In_2Se_3 nanostructures with predominantly {110} facets and photocatalytic degradation of tetracycline.** Appl. Catal. B: Environ., 260 , pp. 118218.

29. Xiong H, Du S, Ni J, Zhou J, Yao J (2016). **Mitochondria and nuclei dual-targeted heterogeneous hydroxyapatite nanoparticles for enhancing therapeutic efficacy of doxorubicin.** Biomaterials, 94 , pp. 70-83.
30. Xia X, Shen J, Cao F, Wang C, Tang M, Zhang Q, Wei S (2019). **A facile synthesis of hydroxyapatite for effective removal strontium ion.** J. Hazard. Mater., 368, pp. 326-335.
31. Xia X, Chen J, Shen J, Huang D, Duan P, Zou G (2018). **Synthesis of hollow structural hydroxyapatite with different morphologies using calcium carbonate as hard template.** Adv. Powder Technol., 29 , pp. 1562-1570.
32. Xiong H, Zou D, Zhou D, Dong S, Wang J, Rittmann BE (2017). **Enhancing degradation and mineralization of tetracycline using intimately coupled photocatalysis and biodegradation (ICPB).** Chem. Eng. J., 316, pp. 7-14.
33. Yi Z, Wang K, Tian J, Shu Y, Yang J, Xiao W, Li B, Liao X (2016). **Hierarchical porous hydroxyapatite fibers with a hollow structure as drug delivery carriers.** Ceram. Int., 42 , pp. 19079-19085.
34. Yu J, Kiwi J, Zivkovic I, Rønnow HM, Wang T, Rtimi S (2019). **Quantification of the local magnetized nanotube domains accelerating the photocatalytic removal of the emerging pollutant tetracycline.** Appl. Catal. B: Environ., 248, pp. 450-458.
35. Yadav S, Singh P, Pyare R (2020). **Synthesis, characterization, mechanical and biological properties of biocomposite based on zirconia containing 1393 bioactive glass with hydroxyapatite.** Ceram. Int., 46 , pp. 10442-10451.
36. Yang Z, Yu X, Lu Z, Li S, Hermansson K (2009). **Oxygen vacancy pairs on CeO_2(110): A DFT+U study.** Phys. Lett. A, 373 , pp. 2786-2792.
37. Zhou Y, Gao Y, Jiang J, Shen YM, Pang SY, Wang Z, Duan J, Guo Q, Guan C, Ma J (2020). **Transformation of tetracycline antibiotics during water treatment with unactivated peroxymonosulfate.** Chem. Eng. J, 379 , pp. 122378.
38. Zhao J, Li Y, Li Y, Yang H, Hu D, Jin B, Li Y (2019). **Application of humic acid changes the microbial communities and inhibits the expression of tetracycline resistance genes in 4-chlorophenol wastewater treatment.** J. Environ. Manage., 250, pp. 109463.
39. Zhang Y, Zhou J, Chen J, Feng X, Cai W (2020). **Rapid degradation of tetracycline hydrochloride by heterogeneous photocatalysis coupling persulfate oxidation with MIL-53(Fe) under visible light irradiation.** J. Hazard. Mater., 392 , pp. 122315.
40. Zhang Y, Zhou J, Chen X., Wang L, Cai W (2019). **Coupling of heterogeneous advanced oxidation processes and photocatalysis in efficient degradation of tetracycline hydrochloride by Fe-based MOFs: Synergistic effect and degradation pathway.** Chem. Eng. J., 369, pp. 745-757.
41. Zhang Y, Gao J, Chen Z, Lu Z (2018). **Enhanced photocatalytic performance of $Bi_4Ti_3O_{12}$ nanosheets synthesized by a self-catalyzed fast reaction process.** Ceram. Int., 44 , pp. 23014-23023.
42. Zhang YC, Li Z, Zhang L, Pan L, Zhang X, Wang L, Fazale A, Zou JJ (2018). **Role of oxygen vacancies in photocatalytic water oxidation on ceria oxide: Experiment and DFT studies.** Appl. Catal. B: Environ., 224, pp. 101-108.

Figures

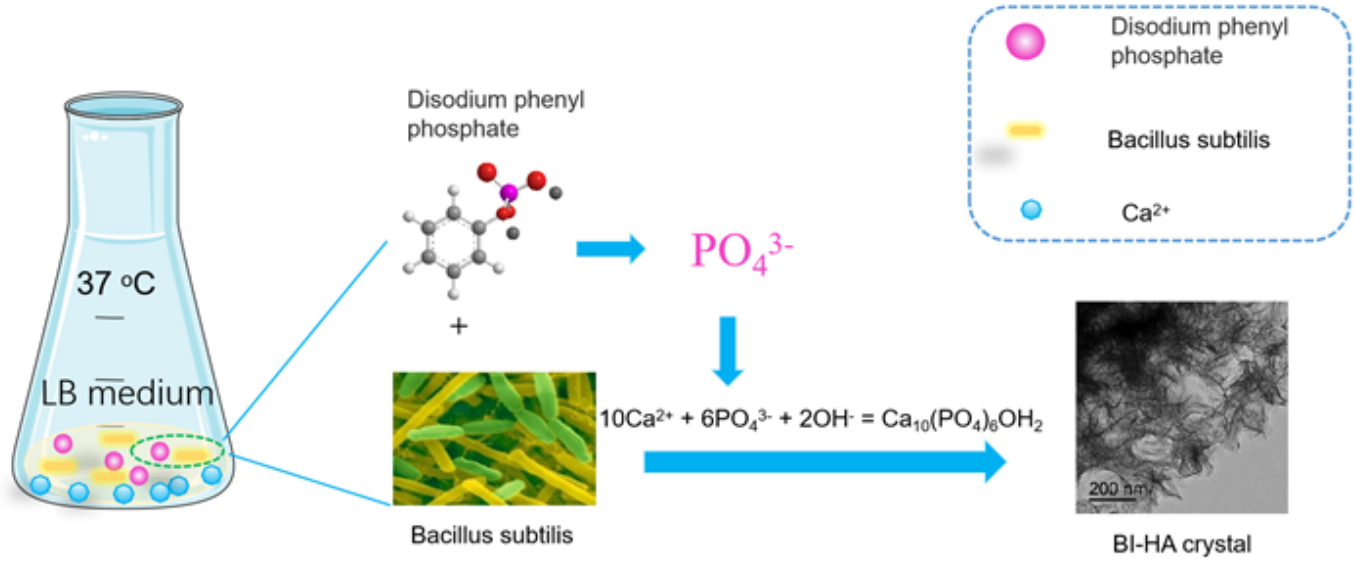

Figure 1

Mechanism of synthesis of the BI-HA products induced by Bacillus subtilis.

Figure 2

SEM images of BI-HA prepared under different calcium ion concentrations: (a) 0.01 mol L−1, (b) 0.03 mol L−1, (c) 0.05 mol L−1, and (d) 0.10 mol L−1. TEM (e) and HRTEM (f) images of BI-HA prepared under calcium ion concentrations 0.10 mol L−1.

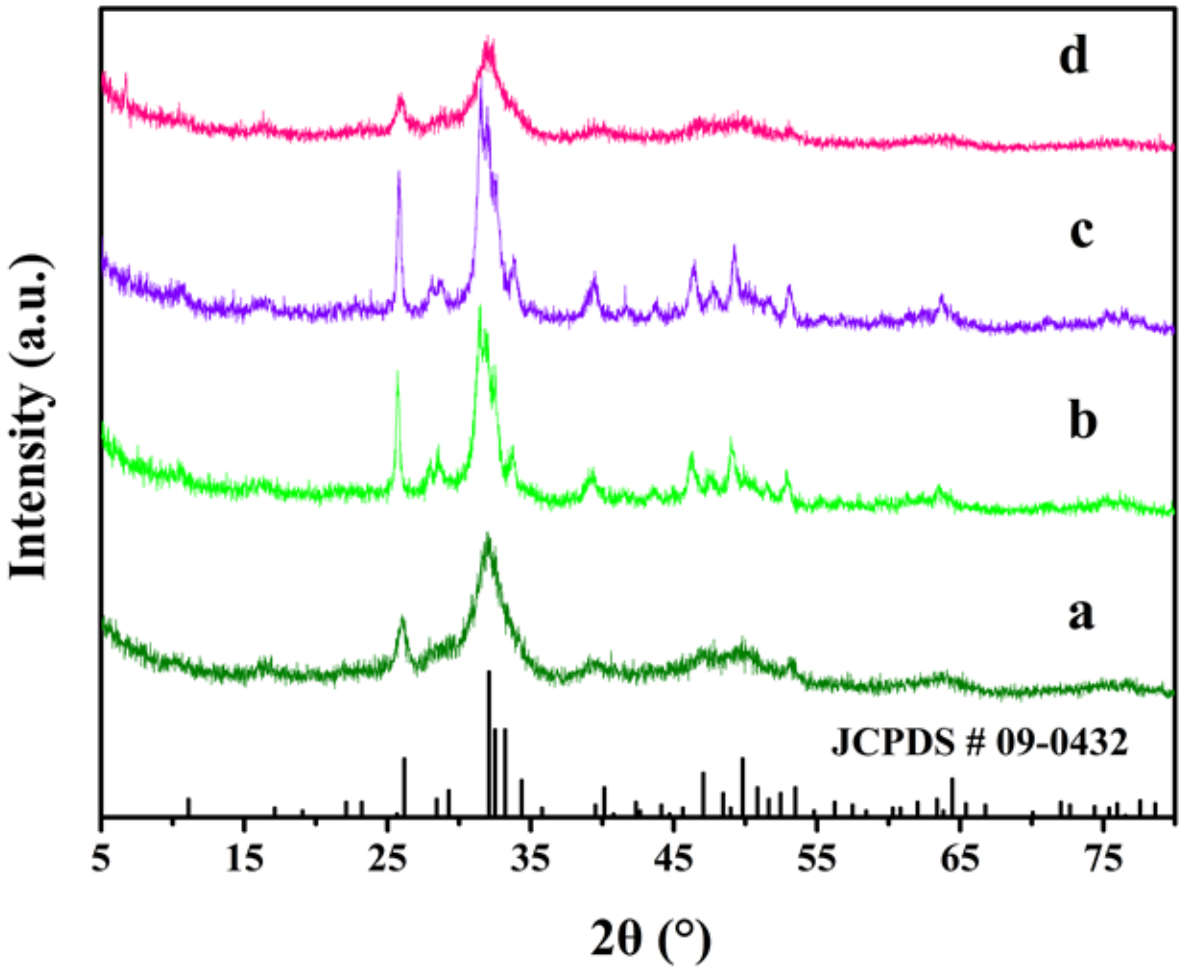

Figure 3

XRD patterns of BI-HA prepared under different calcium ion concentrations: (a) 0.01 mol L−1, (b) 0.03 mol L−1, (c) 0.05 mol L−1, and (d) 0.10 mol L−1

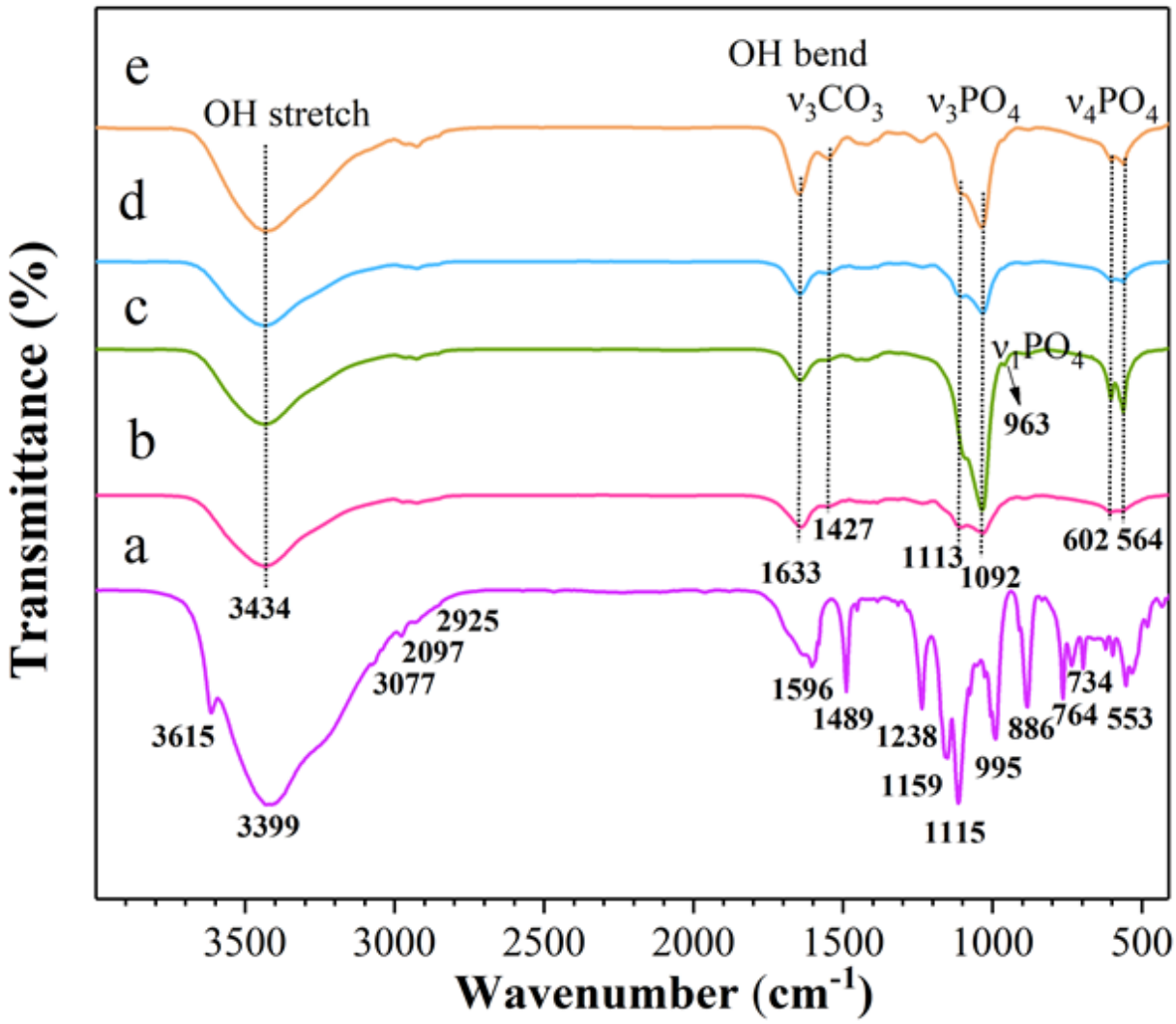

Figure 4

FT-IR spectra of (a) disodium phenyl phosphate dihydrate and BI-HA prepared under different calcium ion concentrations: (a), (b) 0.01 mol L−1, (c) 0.03 mol L−1, (d) 0.05 mol L−1, and (e) 0.10 mol L−1

Figure 5

Nitrogen adsorption, desorption isotherms and the corresponding BJH pore size distribution curves of BI-HA prepared under different calcium ion concentrations: (a, a1) 0.01 mol L−1, (b, b1) 0.03 mol L−1, (c, c1) 0.05 mol L−1, and (d, d1) 0.10 mol L−1

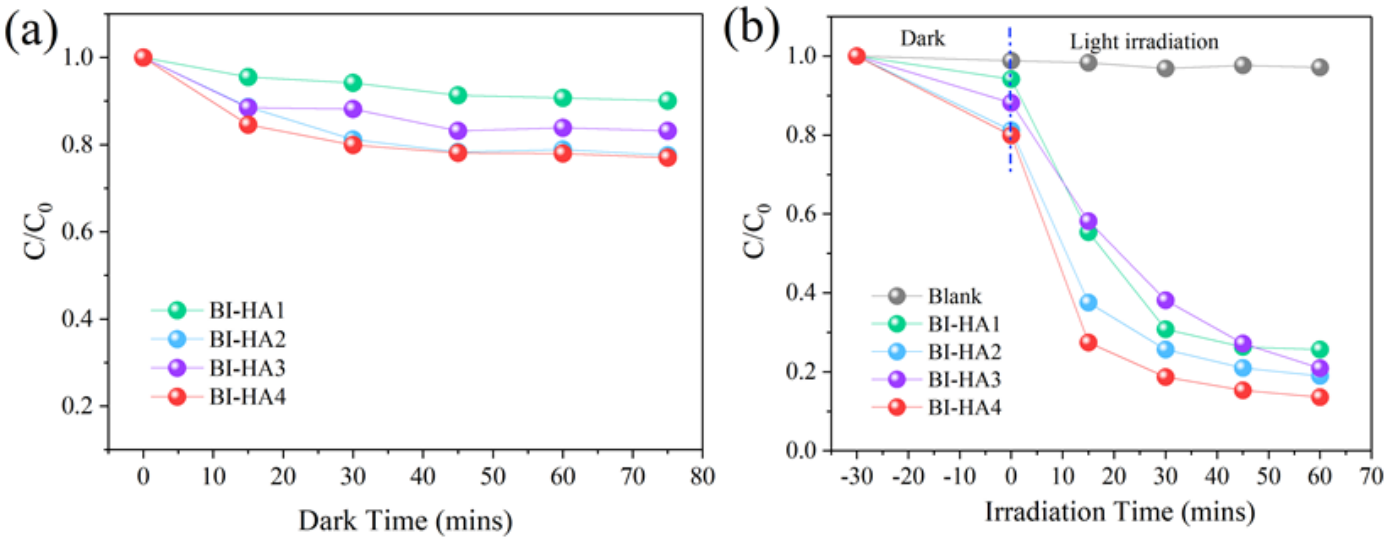

Figure 6

Dark reaction (a) and photocatalytic degradation (b) of TC by as-prepared catalysts.

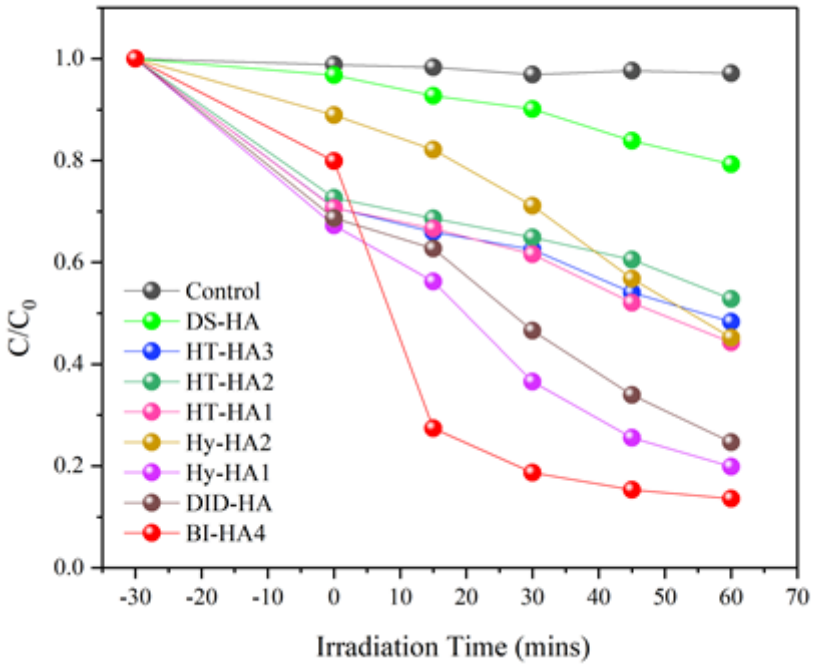

Figure 7

Photocatalytic degradation of TC by as-prepared different HA catalysts with different crystallite structures and morphologies.

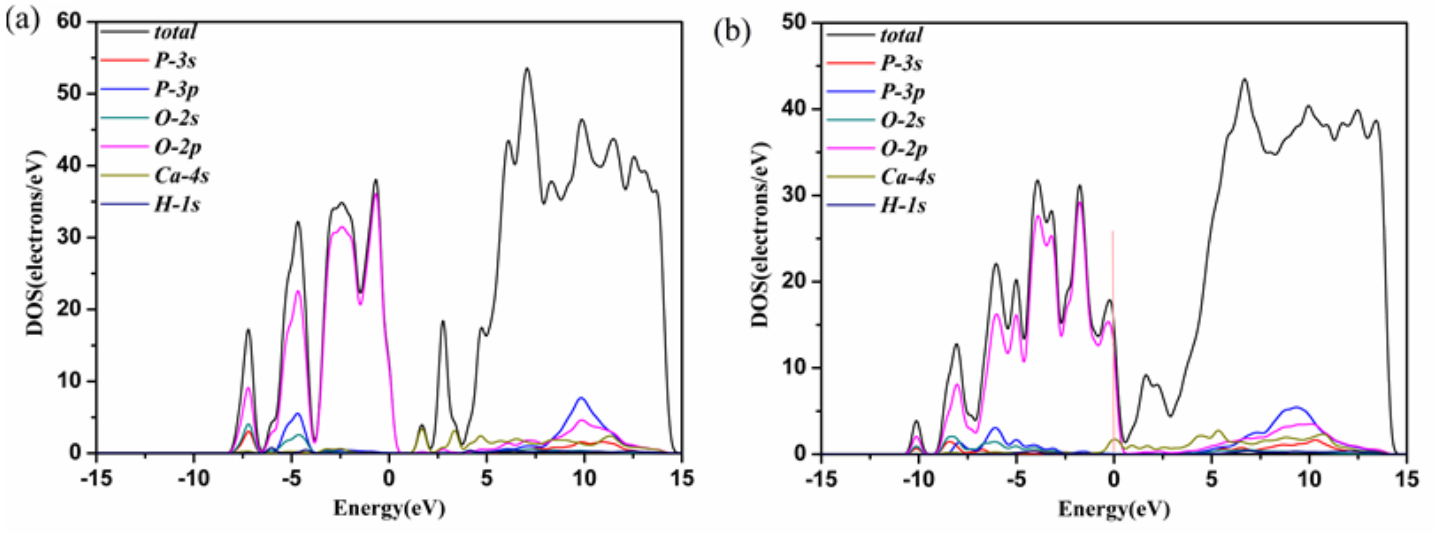

Figure 8

Total density of states (DOS) and projected density of states (PDOS) of (a) HA (001) and (b) HA (100). The dotted lines at energy zero represent the Fermi level.